J Mater Sci (2011) 46:6465–6483
DOI 10.1007/s10853-011-5720-4

REVIEW

Nanoscale volume diffusion

Diffusion in thin films, multilayers and nanoobjects (hollow nanoparticles)

Zoltán Erdélyi · Dezső L. Beke

Received: 2 May 2011 / Accepted: 14 June 2011 / Published online: 1 July 2011
© Springer Science+Business Media, LLC 2011

Abstract Diffusion on the nano/atomic scales in multilayers, thin films has many challenging features even if the role of structural defects (grain-boundaries, dislocations, etc.) can be neglected and 'only' the effects related to the nano/atomic scale raise. This can be the case for diffusion in amorphous materials, in epitaxial, highly ideal thin films, or multilayers where diffusion along short circuits can be ignored and 'only' fundamental difficulties related to nanoscale effects are important. The objective of this article is to review some interesting fundamental experimental and theoretical results in the field of nanoscale volume diffusion in planar and spherical geometries.

Introduction

The first mathematical description of diffusion was given by Fick more than 150 years ago [1, 2].

His first equation relates the flux (**j**: number of atoms crossing a unit area per unit time) to the gradient of the concentration (ρ: number of atoms per unit volume) via the diffusion coefficient (for cubic crystals and isotropic media) D:

$$\mathbf{j} = -D \mathrm{grad}\rho. \tag{1}$$

This equation permits to determine the diffusion coefficient in cases, where the concentration gradient is time independent (steady state regime). In non steady state regime, the diffusion flux and concentration are function of time and position.

In order to be able to determine the diffusion coefficient, it is necessary to take into account the conservation of matter. For not interacting particles (no chemical reaction, no reactions between different types of sites in a crystal, etc.), this is the continuity equation. Combining Eq. 1 and the continuity equations, one obtains Fick's second law:

$$\frac{\partial \rho}{\partial t} = \mathrm{div}(D \mathrm{grad}\rho). \tag{2}$$

Moreover, if the concentration varies only in the x direction:

$$j = -D\frac{\partial \rho}{\partial x}, \tag{3}$$

and Eq. 2 reduces to:

$$\frac{\partial \rho}{\partial t} = \frac{\partial}{\partial x}\left(D\frac{\partial \rho}{\partial x}\right). \tag{4}$$

If, additionally, the diffusion coefficient is *independent of the concentration*, Eq. 4 can be written in the following form:

$$\frac{\partial \rho}{\partial t} = D\frac{\partial^2 \rho}{\partial x^2}. \tag{5}$$

From mathematical point of view, Eq. 5 is a second order, linear partial differential equation. Initial and boundary conditions are necessary to solve it [3–5]. Equation 4 is, however, a nonlinear partial differential equation, which, in general, needs numerical methods to solve.

Introducing the $\lambda = x/\sqrt{t}$ parameter—known as Boltzmann's transformation [4, 5]—the partial differential Eq. 3 transforms to an ordinary differential equation:

Z. Erdélyi (✉) · D. L. Beke
Department of Solid State Physics, University of Debrecen,
P. O. Box. 2, Debrecen 4010, Hungary
e-mail: zerdelyi@dragon.unideb.hu
URL: http://dragon.unideb.hu/~zerdelyi

$$-\frac{\lambda}{2}\frac{d\rho}{d\lambda}=\frac{d}{d\lambda}\left(D\frac{d\rho}{d\lambda}\right), \quad (6)$$

i.e., the composition depends only on λ.[1] From this it follows that a plane with constant composition shifts proportionally to the square root of the time:

$$\rho\left(\frac{x}{\sqrt{t}}\right)=\text{const}\Rightarrow\frac{x}{\sqrt{t}}=\text{const}\Rightarrow x\propto\sqrt{t}. \quad (7)$$

The $x \propto \sqrt{t}$ relation is often called as *parabolic law*, since $x^2 \propto t$.

The most fundamental question related to nanoscale diffusion is if this theory down to which length and time-scale can be applied. Since, as follows from expression (7), for example the shift velocity of a plane with constant composition (e.g., an interface) tends to infinite as the time tends to zero:

$$v_x=\frac{dx}{dt}\propto\frac{1}{2\sqrt{t}}\Rightarrow\lim_{t\to 0}v_x=\infty. \quad (8)$$

This also means that growth rate of the diffusion zone growth at an infinitely fast rate when t goes to zero. Moreover, in the expression (3) of the atomic flux, the gradient is infinite if there is discontinuity in the density at the beginning (typical in interdiffusion measurements).

To overcome the problems related to continuum theories, one may apply discrete/atomistic models, such as kinetic mean filed (KMF, also referred as deterministic kinetic [6]), kinetic Monte Carlo (KMC), molecular dynamics (MD) [7].

However, while continuum models require usually macroscopically defined and measurable input parameters (for instance Fick's equations, diffusion coefficient), atomistic models need microscopic ones, such as jump probability, interaction potentials, etc., which cannot be measured usually (an rather can be estimated indirectly from experimental data).

Another problem is that stress effects—originating for example form net volume transport, difference in thermal expansion of materials, lattice mismatch at interfaces, etc.,—may play very important role in nanoscale diffusion. Stress effects are, however, long-range interaction, whereas atomistic models operate only with short-range interactions. For this reason we are not aware of any atomistic model able to consider stress effects accurately. The inclusion of stress effects in continuum models is, however, quite straightforward in the framework of linear elasticity [8, 9].

The objective of this review article is to present results of efforts trying to reveal the problems of nanoscale volume diffusion and the crossover between the nano- and microscale, i.e., the discrete and continuum models.

[1] This transformation can be done if both the initial and boundary conditions can also be expressed as the function of λ.

Discrete to continuum equations

Researchers are continuously trying to relate discrete and continuum models to each other for different reasons. For example they hope better understanding of the transition between the "continuous/microscopic and discrete/nano world", amelioration of the models, creation of multiscale models, clearing up the atomistic meaning of phenomenological parameters, etc. and also for pedagogical purposes.

Thus, we can find several sources in the literature dealing with this problem (see, e.g., [4, 10, 11]).

These works usually consider very simple cases for the sake of simplicity: unidirectional diffusion, restricted to the flux of atoms between neighboring plans, k and $k+1$, in a simple cubic lattice with interplanar spacing a (Fig. 1). The flux between the planes k and $k+1$ is:

$$j^{k,k+1}=n^k\Gamma^{k\to k+1}-n^{k+1}\Gamma^{k+1\to k}, \quad (9)$$

where $\Gamma^{i\to j}$ is the jump frequency from plane i to plane j and n^k is the number of atoms of diffusion species per unit area on plane k ($n^k/a=\rho^k$, the concentration in atoms per unit volume).

In order to gain a continuum expression for the flux through the plane in the middle between planes k and $k+1$, the quantities n^k and n^{k+1} can be expressed as a function of the continuous variable n and its gradient (higher order terms are neglected):

$$n^k=n(x)-\frac{a}{2}\frac{dn}{dx};\quad n^{k+1}=n(x)+\frac{a}{2}\frac{dn}{dx}. \quad (10)$$

Here $n(x)$ is the value of n in the middle between the planes k and $k+1$. The flux is then:

$$j^{k,k+1}=-\frac{1}{2}a\left(\Gamma^{k\to k+1}+\Gamma^{k+1\to k}\right)\frac{dn}{dx}+n(x)\left(\Gamma^{k\to k+1}-\Gamma^{k+1\to k}\right).$$

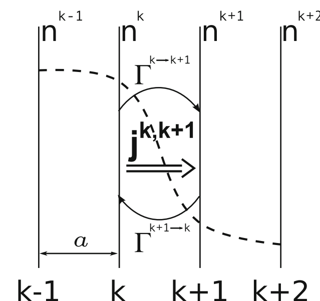

Fig. 1 Unidirectional diffusion, restricted to the flux of atoms between neighboring plans (see also the text)

Changing to units of volume concentration:

$$j(x) = -D(x)\frac{\mathrm{d}\rho}{\mathrm{d}x} + \rho v(x), \tag{11}$$

with

$$\begin{aligned} D(x) &= \frac{1}{2}a^2\left(\Gamma^{k\to k+1} + \Gamma^{k+1\to k}\right) \\ v(x) &= a\left(\Gamma^{k\to k+1} - \Gamma^{k+1\to k}\right), \end{aligned} \tag{12}$$

where $D(x)$ is the diffusion coefficient and $v(x)$ is the drift velocity. Equation 11 is just Fick's first law including the drift term.

We must, however, note that the above derivation supposes that atoms can always jump, i.e., for example interstitial diffusion in dilute case, when a jumping interstitial atom has only vacant neighbouring sites. However, if this cannot be supposed, for example in case of diffusion via vacancy or exchange mechanism (which are still simple mechanisms), a more complicated model is needed.

In case of vacancy mechanism, for example, the flux form plane k to $k+1$ is influenced not only by the jump frequency and the number of atoms of diffusion species per unit area on plane k but also by the number of vacancies per unit area on plane $k+1$. More exactly the *net* flux of diffusion species i between the planes k and $k+1$ is:

$$J_i^{k,k+1} = z_v\left(c_i^k c_v^{k+1}\Gamma_i^{k\to k+1} - c_i^{k+1}c_v^k\Gamma_i^{k+1\to k}\right). \tag{13}$$

Here c_i^k is the probability that and arbitrarily chosen atom on the plane k is an i atom; c_v^{k+1} is the probability that at least one of the z_v neighboring site on the plane $k+1$ of this atom is vacant, which is necessary for the jump of the i atom; and the probability for the jump is $\Gamma_i^{k\to k+1}$.[2] Similarly, an i atom is chosen with a probability of c_i^{k+1} on the plane $k+1$, has a vacant neighbouring site on the plane k with a probability of $z_v c_v^k$ and jumps with a probability of $\Gamma_i^{k+1\to k}$. In other words, $\Gamma_i^{k\to k+1}$ is the jump frequency of diffusion species i from plane k to plane $k+1$ and c_i^k as well as c_v^k are the atomic fractions of diffusion species i and that of vacancies, respectively, on plane k and z_v is the vertical coordination number. Note that the atomic flux $j^{k,k+1}$ is calculated as $J^{k,k+1}N/A$, where N is the number of lattice sites on a plane and A is the area of the specimen perpendicular to the direction of the diffusion.

Similarly to the previous case, after expressing c_i^k, c_i^{k+1} and c_v^k, c_v^{k+1} as a function of the continuous variables c_i, c_v and their gradients, we get for the net flux:

$$\begin{aligned} J_i^{k,k+1} = &-\frac{1}{2}z_v a c_v(x)\left(\Gamma_i^{k\to k+1} + \Gamma_i^{k+1\to k}\right)\frac{\mathrm{d}c_i}{\mathrm{d}x} \\ &+\frac{1}{2}z_v a c_i\left(\Gamma_v^{k\to k+1} + \Gamma_v^{k+1\to k}\right)\frac{\mathrm{d}c_v}{\mathrm{d}x} \\ &+ z_v\left[c_i(x)c_v(x) - \frac{1}{4}a^2\frac{\mathrm{d}c_i}{\mathrm{d}x}\frac{\mathrm{d}c_v}{\mathrm{d}x}\right] \\ &\times\left(\Gamma^{k\to k+1} - \Gamma^{k+1\to k}\right). \end{aligned} \tag{14}$$

Using that $j_i^{k,k+1} = J_i^{k,k+1}\ N/A = J_i^{k,k+1}\ a\ \rho$ (where $\rho = N/(aA)$, the number of sites per unit volume):

$$\begin{aligned} j_i(x) = -\rho\Bigg\{&D_i(x)\frac{\mathrm{d}c_i}{\mathrm{d}x} - D_{v,i}(x)\frac{\mathrm{d}c_v}{\mathrm{d}x} \\ &- \left[c_i(x) - \frac{1}{4}\frac{a^2}{c_v(x)}\frac{\mathrm{d}c_i}{\mathrm{d}x}\frac{\mathrm{d}c_v}{\mathrm{d}x}\right]v_i(x)\Bigg\}, \end{aligned} \tag{15}$$

with

$$\begin{aligned} D_i(x) &= \frac{1}{2}z_v a^2\left(\Gamma_i^{k\to k+1} + \Gamma_i^{k+1\to k}\right)c_v(x) \\ D_{v,i}(x) &= \frac{1}{2}z_v a^2\left(\Gamma_v^{k\to k+1} + \Gamma_v^{k+1\to k}\right)c_i(x) \\ v_i(x) &= z_v a\left(\Gamma_i^{k\to k+1} - \Gamma_i^{k+1\to k}\right)c_v(x), \end{aligned} \tag{16}$$

where $D_i(x)$ is the diffusion coefficient and $v_i(x)$ is the drift velocity for the atom i; $D_{v,i}(x)$ is the diffusion coefficient for the vacancy. Equation 15 is just Fick's first law for vacancy mechanism including the drift term (usually the term including a^2 is negligible).

Similarly, for exchange mechanism, in a binary alloy, very similar expressions can be obtained.

We end this section by inquiring into the physical significance of the drift velocity. Since, by definition, v is proportional to the difference in jump frequencies, it is thus a measure of the "bias" in the system, a bias that exists even if the particles are evenly distributed among sites. This bias is, in general, related to a potential force field V acting on the diffusion species with a force $F = -\nabla V$. These fields can be internal (e.g., chemical, diffusion-induced stress) or caused externally by applied fields (e.g., electric filed acting on charged particles, gravitation, external stress). The bias can usually be expressed in the jump frequencies by the following form:

$$\begin{aligned} \Gamma_i^{k\to k+1} &= \Gamma_i(x)\exp\left[+\frac{\varepsilon_i(x)}{2k_BT}\right] \\ \Gamma_i^{k+1\to k} &= \Gamma_i(x)\exp\left[-\frac{\varepsilon_i(x)}{2k_BT}\right]. \end{aligned} \tag{17}$$

Here $\Gamma_i(x)$ is the jump frequency without driving forces, $\varepsilon_i(x)$ equals the work done by the driving force F over the distance a between the planes k and $k+1$ (i.e., $\varepsilon_i(x) = aF = -a\nabla V$), k_B is Boltzmann's constant and T is the absolute temperature. Thus, e.g., according to Eq. 16:

[2] Although usually it is not explicitly declared, z_v is included in Γ in Eqs. 9–12. From Eq. 13, z_v is not included in Γ.

$$D_i(x) = z_v a^2 \Gamma_i(x) \cosh\left[+\frac{\varepsilon_i(x)}{2k_BT}\right] c_v(x)$$
$$v_i(x) = 2z_v a \Gamma_i(x) \sinh\left[+\frac{\varepsilon_i(x)}{2k_BT}\right] c_v(x). \tag{18}$$

Finally we note, that $\Gamma_i(x)$ has, in general, an Arrhenius-type temperature dependence:

$$\Gamma_i(x) = v \exp\left[-\frac{E_i(x)}{k_BT}\right], \tag{19}$$

where v is the attempt frequency and $E_i(x)$ is activation energy of a jump.

For example in the framework of a kinetic mean filed model using exchange mechanism in a binary solid [6], $\Gamma^{k\to k+1}$, i.e., the activation energy for a the exchange of an A and B atoms in plane k and $k+1$, respectively, can be given by [12]:

$$\Gamma^{k\to k+1} = v \exp\left[-\frac{\hat{E}^0 - \alpha^k + \epsilon^k}{k_BT}\right], \tag{20}$$

with

$$\alpha^k = \left[z_v(c^{k-1} + c^{k+1} + c^k + c^{k+2}) + z_l(c^k + c^{k+1})\right]M,$$
$$\varepsilon^k = \left[z_v(c^{k-1} + c^{k+1} - c^k - c^{k+2}) + z_l(c^k - c^{k+1})\right]V. \tag{21}$$

where z_l is the number of neighboring sites on plane i, c^k is the atomic fractions of A atoms on plane $k, \hat{E}^0$ is the composition independent part of the activation energy. M and V can be calculated form the pair interaction energies V_{XY}: $M = (V_{AA} - V_{BB})/2$ and $V = V_{AB} - (V_{AA} + V_{BB})/2$. As will be discussed below, M determines the strength of the composition dependence of the diffusion coefficients, whereas V is the regular solid solution parameter, proportional to the heat of mixing and measures the phase separating ($V > 0$) or the ordering ($V < 0$) tendency.

Validity limit of continuum equations

We have seen that the continuum and discrete equations can be transformed into each other. It is, however, clear that there is a certain difference between the continuum and the discrete descriptions due to the approximations used for the interpolation of the composition (Taylor expansion). It is easy to show throughout the example of the time evolution of a cosinusoidal composition modulation (see, e.g., [13]):

$$\rho(x,t) = \rho_0 + A(t)\cos(2\pi x/\Lambda), \tag{22}$$

where Λ is the wavelength of the modulation, $A(t)$ is the amplitude and ρ_0 is the average value of ρ. Supposing composition independent diffusion coefficient and substituting Eq. 22 into Fick's second equation (Eq. 5) and its discrete form:

$$\frac{\partial \rho^k}{\partial t} = D\frac{\rho^{k+1} + \rho^{k-1} - 2\rho^k)}{a^2} \tag{23}$$

and then solving the obtained differential equations, we arrive to the following expressions:

$$\frac{\mathrm{d}}{\mathrm{d}t}\ln A(t) = -Dh^2 \quad \text{with} \quad h^2 = (2\pi a/\Lambda)^2 \tag{24}$$

for the continuum, and

$$\frac{\mathrm{d}}{\mathrm{d}t}\ln A(t) = -DH^2 \quad \text{with} \quad H^2 = (2/a^2)[1 - \cos(2\pi a/\Lambda)]. \tag{25}$$

for the discrete case. This means that equations and (25) give the same result only if h^2 and H^2 (or h^2a^2 and H^2a^2) coincide (see Fig. 2).

Historically, Cook et al. [13] showed in 1969 that the continuum and discrete approximations give the same results only if the wavelength of the modulation Λ is at least six times longer than the interatomic distance, a, in the direction of the diffusion ($\Lambda > 6d$). Cahn [14], Yamauchi and Hilliard [15] in 1972 found similar range of validity of the continuum approach for intermixing of multilayers. These conclusions, however, are obtained in linear approximation, i.e., assuming that the diffusion coefficient is independent of concentration. The treatment

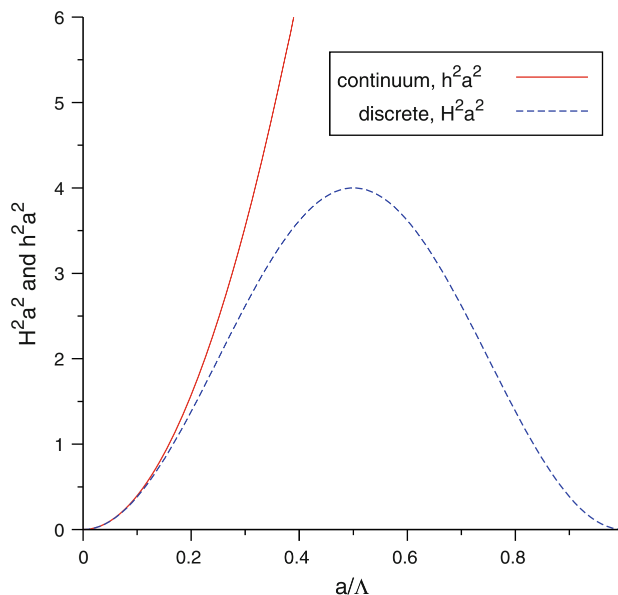

Fig. 2 The solution of the continuum and the discrete form of Fick's second equation for composition independent diffusion coefficient is the same where h^2a^2 and H^2a^2 coincide, i.e., approximately for $\Lambda > 10a$

of the effects of this type of nonlinearity is very complicated. Tsakalakos [16, 17], Menon and de Fontaine [18], in the 1980s and the beginning of the 1990s, tried to treat this problem analytically, or by solving the continuum equations numerically, considering a concentration dependence no stronger than a quadratic one in the diffusion coefficient, although even in ideal solutions it can be stronger and is better described by an exponential dependence. More recently, in 1999, Erdélyi et al. [19] showed—by solving the continuous and discrete forms of Fick's equations numerically for a multilayer geometry—that in case of an exponential dependence of the diffusion coefficient the discrete and continuum approximations give the same results only if the modulation length of a multilayer is larger than 3–50 nm, i.e., approximately $\Lambda > 6a$–$100a$, depending on the strength of the composition dependence of the diffusion coefficient.

Nanoscale diffusion in thin films and multilayers

Either we use discrete or continuum models to calculate the diffusion processes in diffusion couples, thin films, multlayers, etc., i.e., interdiffusion, in principle we should always take into account that the tracer (random walk or Brownian) diffusion coefficients depends on the local composition. Since the mobility of an A atom in an A matrix usually differs from that in a B matrix, especially at the temperatures used in thin film and multilayer investigations and applications (see tracer diffusion data in [20, 21]). It is quite often that an A atom diffuses orders of magnitude (usually 4 to 7) faster in the B matrix than in the A.

It is very common in the diffusion literature to describe the composition dependence of the diffusion coefficients by an exponential function (e.g., [19]). One of the most accurate experiment to measure the composition (and also temperature) dependence of diffusion coefficients was performed recently by Kube et al. [22]. They measured the composition dependence of Si and Ge in relaxed $Si_{1-x}Ge_x$ alloys. The results are shown in Fig. 3. Using these data the composition dependence of the diffusion coefficients can be plotted easily and as can be seen for example in Fig. 4, the experimental data fit to straight lines on a $\log_{10}D$ versus composition plot very well, which means that the diffusion coefficients, both for Si and Ge, depends exponentially on the composition.

In an AB binary system one has to distinguish between the (tracer) diffusion coefficients of A and B atoms: $D_A = D_A^0 \exp(m_A c_A)$ and $D_B = D_B^0 \exp(m_B c_A)$, where D_A^0 as well as D_B^0 are composition independent factors, c_A is the composition of the A atoms, m_A and m_B are parameters determining the strength of the composition dependence. It is worth introducing the $m_A' = m_A \log_{10}e$ and $m_B' = m_B \log_{10}e$ parameters (e is the base of natural logarithm), which give in orders of magnitude the ratios of the diffusion coefficients in the pure A and B matrixes. For instance, $m_A' = 4$ means that the A atoms jumps 10,000 times faster in the A matrix than in the B. Accordingly, m_A' and m_B'

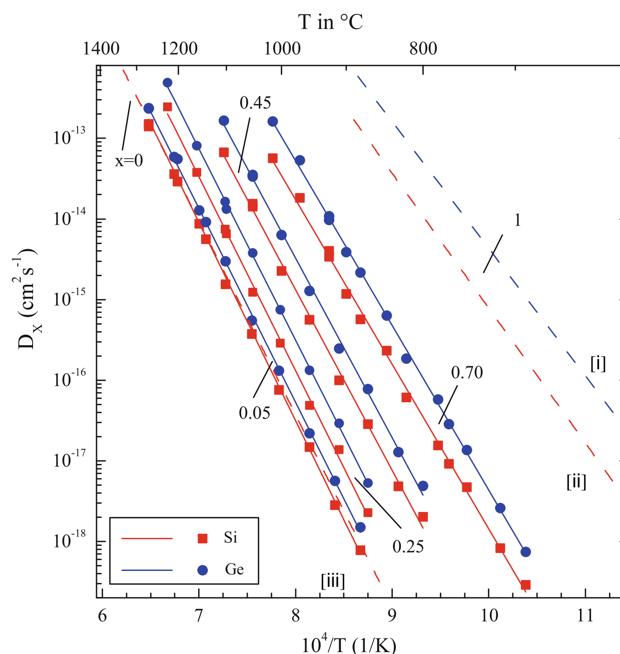

Fig. 3 Temperature dependence of the diffusion coefficient of Si and Ge in $Si_{1-x}Ge_x$. For comparison the lower, second upper, and upper *dashed lines* show the temperature dependence of Si self-diffusion ([iii] = Refs. [23, 24]), Si diffusion in Ge ([ii] = Ref. [25]), and Ge self-diffusion ([i] = Ref. [26]),respectively (after Fig. 2 in [22])

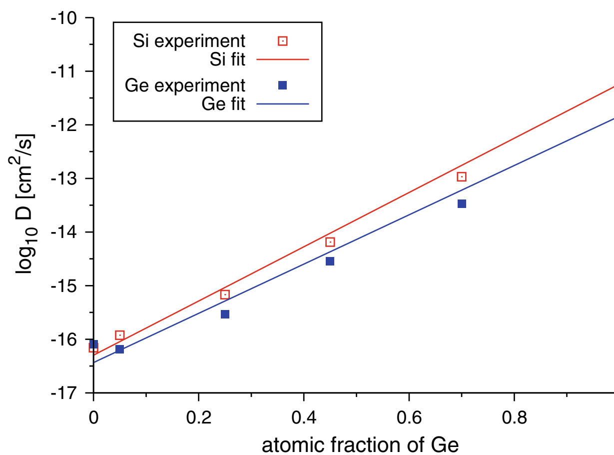

Fig. 4 Composition dependence of diffusion coefficients of Si and Ge in SiGe alloy at 1273 K (created using the data in [22]). The experimental data fit to straight lines on a $\log_{10}D$ versus composition plot, which means that the diffusion coefficients, both for Si and Ge, depends exponentially on the composition. The slope of the straight lines gives the values of the $m'_{Si} = 5.06$ and $m'_{Ge} = 4.60$ parameters describing the strength of the composition dependence (see also the text)

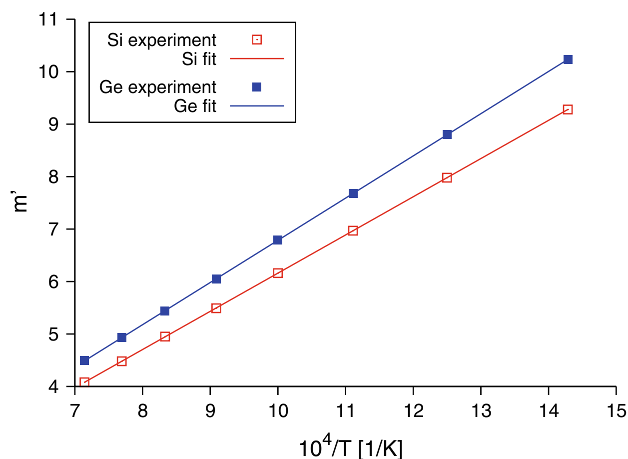

Fig. 5 Temperature dependence of the diffusion asymmetry parameters Si (m'_{Si}) and Ge (m'_{Ge}) in $Si_{1-x}Ge_x$. The data points are obtained after analysing the data in Fig. 2 of [22]), and fit to straight lines

parameters can be obtained from the ratio of the corresponding diffusion coefficients, e.g., $m'_A = \log_{10}\frac{D_{AinA}}{D_{AinB}}$ (and can also be called as *diffusion asymmetry* parameters). Note that in many cases, for the sake of simplicity, it may be supposed that $m_A' = m_B'$, i.e., only one parameter (m') describes the strength of the diffusion asymmetry (see also, e.g., Fig. 4).[3]

Typically the value of m' lies in the range of 4–7 at temperatures where thin film and multilayer experiments are performed. Analysing the data shown in Fig. 3, we obtain for example that m' varies in the range of 4–10 in the temperature range of 700–1400 K (see Fig. 5). It is worth mentioning that if D has Arrhenius-type temperature dependence and exponential composition dependence, m' is inversely proportional to T: $\log_{10} D \propto 1/T$ and also $\log_{10} D \propto mc$, then $m \propto 1/T$ [see also Eqs. 20 and 21].

Although the exponential composition dependence of D is in accordance with experimental observations and the form of composition dependence of the jump probabilities or frequencies in atomistic calculations like kinetic Monte Carlo or kinetic mean filed technique (e.g., [19, 27, 28]), in principle any other physically relevant function can be used to consider the composition dependence of the diffusivities similarly.

Despite the apparent existence of the composition dependence of the tracer diffusion coefficients, it is often neglected in calculations and interpretation of experimental result. In the next, we will show some interesting nanosacle diffusion phenomena in which the diffusion asymmetry (strong composition dependence of D) plays a key role.

Shift of sharp interface

If we do calculations, either by continuum or atomistic models, both neglecting and considering the composition dependence of the diffusion coefficient, the very first difference we recognise between the results is how the shape of the composition profile evolves in time. The development of the composition profiles is quite symmetrical for composition independent D, whereas, for strong composition-dependent D, the composition profiles are very asymmetric. The interface between the A and B matrixes remains abrupt and shifts until the component in which the diffusion is slower is consumed. It can be seen in Fig. 6 that the Si atoms diffuse very fast into the Ge matrix and are distributed homogeneously, whereas the Ge atoms practically cannot penetrate into the Si matrix, since the

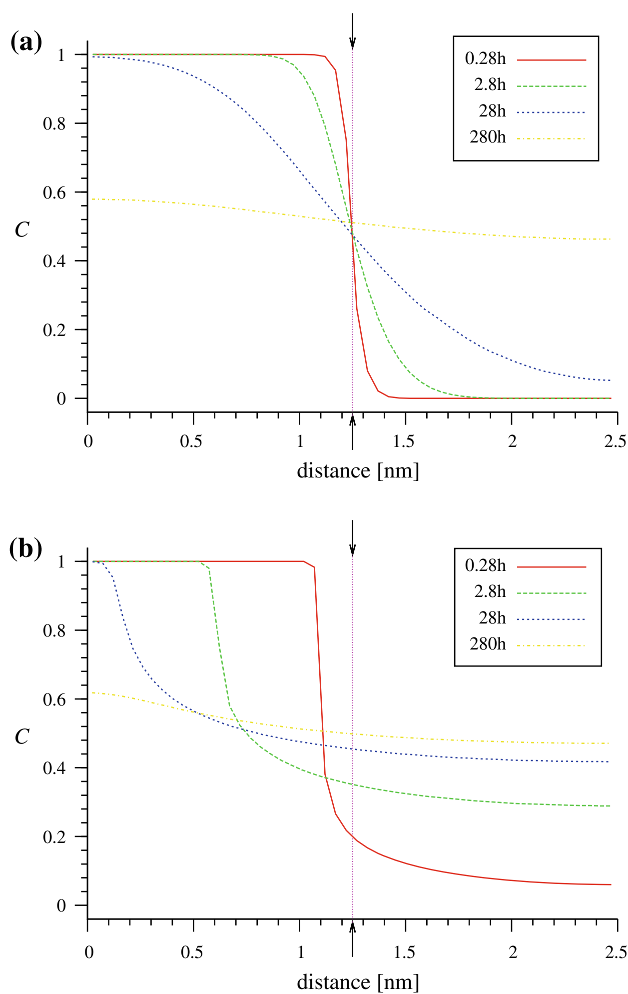

Fig. 6 Composition distributions of Si in a Si/Ge multilayer (only half bilayers are shown for symmetry reasons) at different times for the continuum model. **a** composition independent D, i.e., $m' = 0$ **b** composition dependent D, where $m' = 4$. The *arrows* show the initial position of the interface

[3] It is worth mentioning that $m' = 2ZM/k_BT \log_{10}e$, where $Z = z_l + 2z_v$ and e is the base of the natural logarithm. It also shows that M in Eq. 21 can be determined from diffusion experimental data.

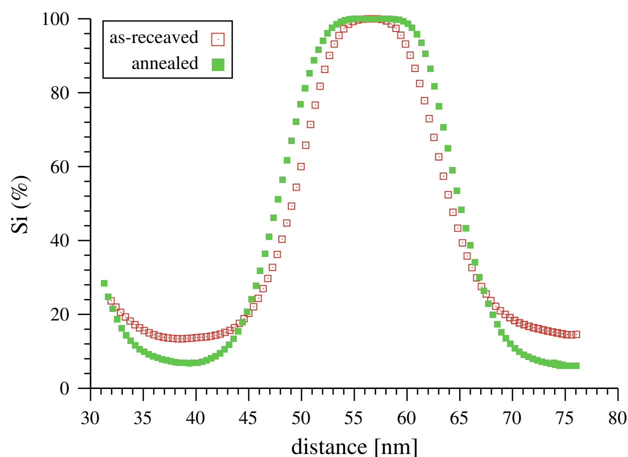

Fig. 7 One period of the composition profiles of the as-received and heat treated amorphous Si/Ge multilayers obtained by Auger depth profiling [29]

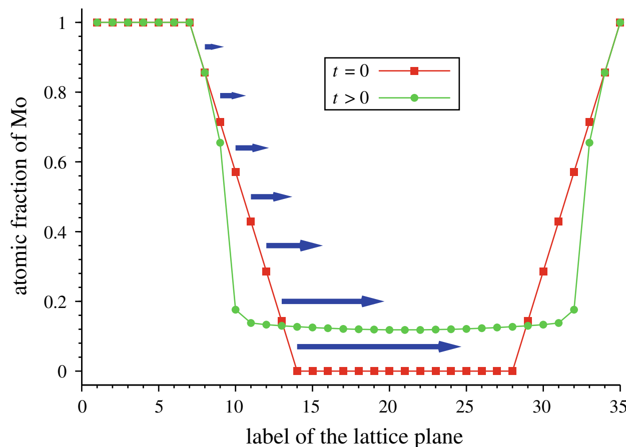

Fig. 8 Composition distribution during intermixing in one period of a Mo/V multilayer calculated by KMF. The *arrows* represent schematically the 'flux distribution', i.e., their lengths are proportional to the absolute value of the atomic flux [32]

diffusion is more than four orders of magnitude faster in the Ge than in the Si.

The asymmetrical intermixing was observed experimentally, e.g., in Si/Ge multilayers [29, 30] (Fig. 7).

Interface sharpening in completely miscible alloys

As was shown by using computer simulations (KMF and KMC) [31] for strongly composition-dependent diffusion coefficients not only sharp interfaces remain sharp but an initially diffuse *A*/*B* interface can become chemically abrupt even in ideal (either crystalline or amorphous) systems with complete mutual solubility.

It is perhaps even more surprising that the sharpening can be qualitatively predicted from the classical Fick first law. Since, in ideal systems, D has a positive value, the direction of the flux is always opposite to the direction of the concentration gradient and, for concentration independent diffusion coefficients, this equation should lead to flattening of the interface. However, if the diffusion coefficient composition dependent, $D = D(c)$, the flux j depends not only on the concentration gradient but also on the local composition of the sample. Figure 8 illustrates the 'flux distribution' at the interface in the initial state, when the matrixes are separated by a wide interface. As the concentration gradient is constant along the interface then, according to Fick's first law, it is only D on which the absolute value of the atomic flux depends and the 'flux distribution' follows the $D = D(c)$ function.

It was also shown, using Stephenson's continuum model, that sharpening takes place where stress effects intervene [33] (see also Stress effects section). Later on Roussel and Bellon [34] investigated how the diffusion mechanism and the short-range order influence the sharpening.

The predicted phenomenon was proved experimentally in epitaxially grown Mo/V multilayers by in-situ synchrotron measurements [32].

Anomalous (non-Fickian) diffusion kinetics

It is known from Fick's phenomenological laws that, during annealing of a diffusion couple, the p displacement of a plane with constant composition (or an abrupt interface) is proportional to $t^{1/2}$ or $p^2 \propto t$ (Fickian or normal shift kinetics with t equal to time)[4, 5]. This is related to Einstein's relation $\langle R^2 \rangle \propto t$, i.e., the mean square displacement of particles is proportional to the time, since Brownian motion of particles takes place in diffusion processes in ideal or dilute solids (even in other cases, a random walk or Brownian 'part' is included in diffusion coefficients). Ficks equations, however, do not allow modelling of a large number of diffusion phenomena. Departure from Brownian motion appears to be very common, so that anomalous diffusion would actually appear as normal [35].

Several extensions of Fick's theory are described in [36]. One of the most interesting is based on fractional calculus [37]. The main idea is that Ficks second equation can be written in the following form

$$\frac{\partial^\alpha}{\partial t^\alpha}\rho(x,t) = D_\alpha \nabla^2 \rho(x,t), \tag{26}$$

where α is the order of differentiation and can be a fractional number. As a consequence, the diffusion coefficient should also be generalised, because its dimension is length^2/time$^\alpha$, and D_α is called as fractional diffusion coefficient. From the structure of Eq. 26, it follows that the shift of a plane with constant composition—or in general the mean squared displacement of diffusion particles—is

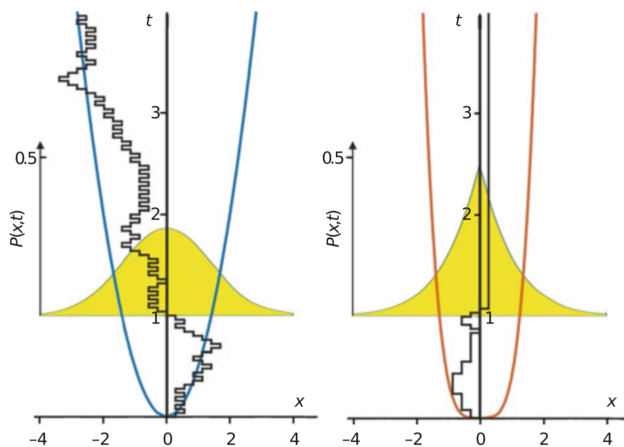

Fig. 9 The *step like/black* lines indicate a specific realization of random walks with $\alpha = 1$ (*left panel*) and 1/2 (*right panel*). In the *right panel*, steps occur very irregularly; most of the time the walker does not move at all. As a consequence, the mean square displacement grows considerably slower than in simple random walks. The *smooth/blue and red* curves indicate the typical behaviour of the displacement: $\langle x^2\rangle^{1/2} \propto t^{1/2}$ for $\alpha = 1$ and for $\langle x^2\rangle^{1/2} \propto t^{1/4}$. The filled *gray/yellow* curves show the probability distributions $P(x, t)$ at $t = 1$. For regular diffusion, which corresponds to the simple random walk, the distribution is Gaussian. For fractional diffusion, its characteristic tent-like form displays a cusp at $x = 0$ [37] (Color figure online)

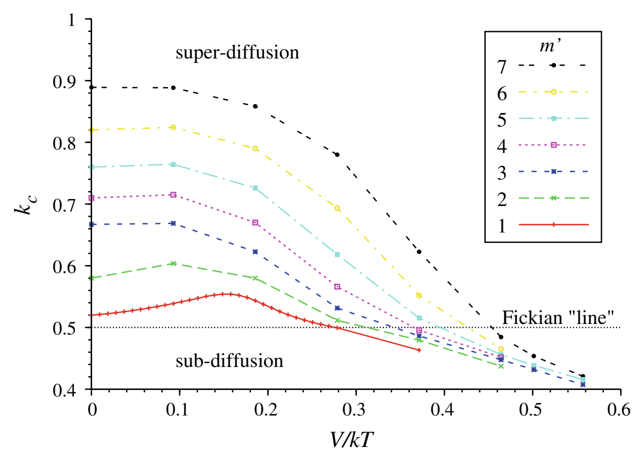

Fig. 10 Kinetic exponent versus V/kT for different m' values. For small m' values k_c is almost constant and is very close to 0.5. The deviation (anomaly) from the Fickian (normal) kinetics increases with increasing m' for a fixed value of V/kT. We can observe both super- and sub-diffusion regimes [38]

proportional to a fractional power of the time $x^2 \propto t^\alpha$ (see Fig. 9). Note that not only the time fractional but space fractional and time-space fractional form of Fick's (or Focker–Planck) equation also exist.

In the followings, we summarise briefly how the composition dependence of the diffusion coefficient influences the diffusion kinetics on the nanoscale.

Erdélyi et al. [38] investigated the position of a plane with constant composition versus time by computer simulation. Potting the logarithm of the position versus the logarithm of the time ($\log p \propto \log t$) and fitting a straight line to the data, its slope gave the power of the function describing the shift of the interface (called *kinetic exponent* and denoted by k_c, which is equal to $\alpha/2$). Obviously for parabolic (normal Fickian) interface shift $k_c = 0.5$. Thus, if the kinetics is non-Fickian, $k_c \neq 0.5$ or the data do not fit on a straight line on the $\log p \propto \log t$ plot. Both the parameters m' and V (or V/k_BT) were changed during the calculations.

Figure 10 shows the initial values of k_c versus V/kT for different m' values. It can be seen that k_c is almost constant and, as expected, is very close to 0.5 for small m'. At the same time, the deviation from the square-root kinetics increases with increasing m' for a fixed value of V/kT.

The deviation from the parabolic law is a real "nano-effect" because, after dissolving a certain number of layers (long time or macroscopic limit), the interface shift returns to the parabolic behaviour independently of the input parameters (see, e.g., Fig. 10). This transition can be understood from the analysis of the atomic currents in the different parts of the sample [39]. In principle three currents can be distinguished: (i) J_α in matrix A, where the diffusion is very slow, (ii) J_I across the interface region, and (iii) J_β in matrix B, where the diffusion is fast (Fig. 12). However, J_α can be neglected, because practically there is no diffusion in matrix A. Moreover, at the beginning of the kinetics, when the composition gradient is very large, the flux in the B-rich phase (β phase) is larger than across the interface ($J_I < J_\beta$). In this stage J_I controls the diffusion. During the process J_β becomes smaller and smaller because the tail of the composition profile in the β phase grows more and more resulting in the decrease of the gradient of the composition. Although, J_I also decreases with increasing time but J_β decreases much faster. As a result, in a certain moment J_β becomes smaller than the J_I, and from this point J_β is the rate limiting (Fig. 11).

As an initially abrupt interface remains sharp if the diffusion asymmetry strong enough or/and the system has a tendency for phase separation, there is a chance to measure the anomalous kinetics in a properly designed experiment. The main idea is to prepare a thin deposit onto the surface of a substrate, where the deposit is thin enough to be able to detect the signal coming from the substrate, i.e., the deposit is "transparent" for the experimental technique used. In this case the thickness of the deposit can be calculated from the ratio of the deposit and substrate signal intensities (I_{dep}/I_{sub}). During annealing, if the interface remains abrupt, from the change of I_{dep}/I_{sub} (I_{dep} decreases, whereas I_{sub} increases in time) it is possible to determine how the thickness of the deposit decreases in time. The deposit thickness can easily be converted to interface position;

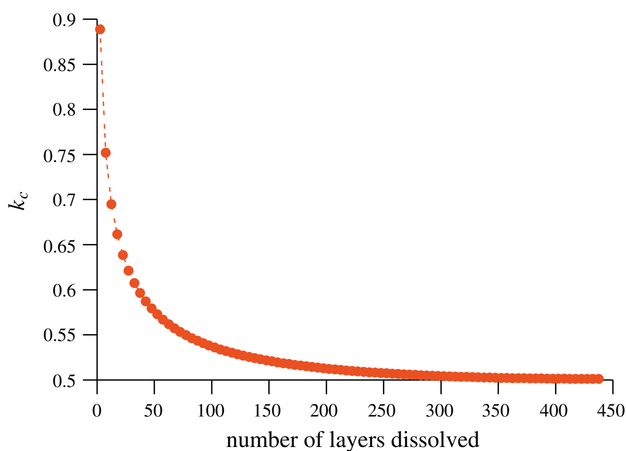

Fig. 11 Change of k_c during dissolution ($m' = 7$, $V/kT = 0.09$). The more the number of layers dissolved, the closer the value of k_c is to 0.5 [38]

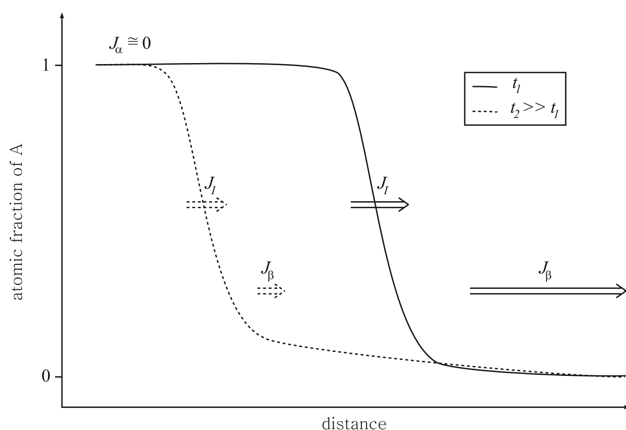

Fig. 12 Scheme of the composition profile and the atomic fluxes in the linear (t_1, *solid line*) and parabolic ($t_2 \gg t_1$, *dashed line*) kinetic regimes. In the linear regime $J_\beta \gg J_I$, whereas in the parabolic one $J_\beta \ll J_I$. The length of the *arrows* illustrates the intensity of the fluxes. Note that for large $|m|$ J_α is practically zero as indicated [39]

i.e., the log $p \propto$ log t function can be plotted, for which the slope is just equal to k_c.

These kind of experiments were performed by AES (Auger electron spectroscopy) and XPS (X-ray photoelectron spectroscopy) techniques in four thin film/substrate systems: Ni/Au(111) (phase-separating) [40], Ni/Cu(111) (completely miscible) [41], Si/Ge(111) (completely miscible) [42], amorphous Si/Ge (completely miscible) [43]. Super-diffusion was found in all the systems with $k_c = 0.6–0.7$, 1, 0.85, and 0.7, respectively.

Furthermore in the amorphous Si/Ge system, not only the anomalous part of the diffusion process could be observed but also the transition back to the classical Fickian behaviour was seen. Initially k_c was found to be 0.7 ± 0.1, whereas in the later domain it was 0.5 (see Fig. 13).

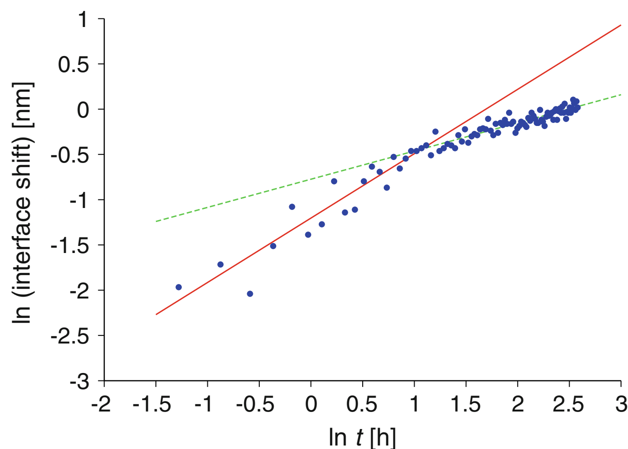

Fig. 13 Interface shift (initial minus apparent thickness of the Si film) in dependence of time on a log–log scale. The non-Fickian first part as well as the transition are clearly visible. (The *solid/red* straight line is fitted to the first anomalous part of the data, whereas the *dashed/green* one to the last Fickian part) [43] (Color figure online)

Although it is almost exclusively accepted in the literature that linear growth kinetics are the result of interface reaction control, these results suggest that the linear (non-Fickian) diffusion kinetics or even the growth of a reaction layer on the nanoscale cannot be automatically interpreted by interface reaction control.

Interface reactions are widely used in metallurgical and microelectronic applications, and there is an increasing need to control them on the nanoscale. Because of the long standing interest in electronic applications, the literature on reactive diffusion in transition metal/silicon systems on micrometer scale is well-documented (see, e.g., Refs. [44] and [45] for review).

Diffusion-reaction kinetics have also been recently investigated on the nanoscale (e.g., [46] and [47]). Nemouchi et al. [46] have investigated experimentally the formation of Ni_2Si in a crystalline Ni/Si couple, whereas Cserháti et al. [47] the formation of CoSi and Co_2Si in crystalline-Co/amorphous-Si multi- and bilayers. They have found close to linear kinetics at the beginning of the phase formation. Nemouchi et al. have treated their results in the framework of the phenomenological linear-parabolic law, i.e., reaction (or interface) control-diffusion control. No physical reasons for the reaction control and the transition to diffusion control have been given. Cserháti et al. [47] have, however, argued, supported by computer simulations, that the diffusion asymmetry may play a significant role in non-Fickian growth kinetics.

On the basis of KMC calculations, Portavoce et al. [48] have, however, found that the phase growth linear time dependence is related neither to an interface effect nor to diffusion asymmetry but results from the first stage of phase formation in a local composition close to the phase

stoichiometry, whereas the following parabolic time dependence is due to the need for atom transport before phase nucleation. Cserháti et al. [47] have investigated experimentally the role of the first stage of phase formation. They have prepared both Co/Si bi- and Co/CoSi/Si trilayer samples and investigated the phase growth kinetics. Although, the first stage of phase formation intervene only in the case of the bilayer samples, they have measured the same kinetics for the growth of the CoSi phase. Moreover, it is interesting to note that in case of diffusion asymmetry—the absence of diffusion asymmetry is extremely rear—the phase formation starts at highly non-stoichiometric composition as was shown by KMC calculations [49], which also influences the first stage of the phase formation.

As can be seen the first stage of phase formation and the origin of the phase growth linear time dependence is still an open question.

Stress effects

As was mentioned in the "Introduction" diffusion-induced stresses can have an important effect on diffusion kinetics on the nanoscale. The characteristic feature of these phenomena is related to the interplay between the Kirkendall-shift, as a special way of relaxation of the interdiffusion induced fields, and the driving forces (field gradients) still remaining present in the sample.

As an example of the interplay of stresses, non-equilibrium vacancies and relaxation by Kirkendall shift, one can consider interdiffusion first in a binary planar system. Here there is a resultant vacancy flow, caused by the inequality of the intrinsic atomic fluxes in the lattice frame of reference, oriented toward the faster component. This resultant volume flow is responsible for the development of stress free strains in the diffusion zone: one side tends to shrink and the other one to expand. Additional stress free strains can also develop due to the difference of the atomic volumes and/or to the formation of intermetallic compounds in which the specific volumes of the constituents can be considerably different than in the parent phases [50]. The partial or full relaxation of these diffusional stresses can lead to the well-known Kirkendall-shift: in case of vacancy mechanism, if the efficiency of the vacancy sources and sinks (e.g., at dislocations) is high enough, atomic planes will be removed/inserted at the corresponding fast/slow component of the diffusion couple. If this process is fast and complete then the stresses will be relaxed and the pure Darken-regime is realized. In this regime, since the interdiffusion coefficient is given by $D = c_A D_B + c_B D_A$ (c_i and D_i for $i = A, B$ denote the atomic fractions and the intrinsic diffusion coefficients, respectively), the overall intermixing in the laboratory frame of reference is controlled by the larger diffusion coefficient, and the Kirkendall velocity is determined by the product of the $D_B - D_A$ difference and the composition gradient. Furthermore the Kirkendall shift is proportional to the square root of time.

In the other limiting case, i.e., when the stresses and/or vacancy supersaturation cannot be relaxed, after a certain set up time, steady state corrections to the initial atomic fluxes should be taken into account. These additional terms to the fluxes are proportional to the diffusion-induced field gradients (gradient of stresses and/or chemical potential due to vacancy supersaturation) and act as dictated by the Le Chatelier-Brown principle: the larger (smaller) flux will be decreased (increased) and in steady state the fluxes will be equal to each other and the sources of diffusion-induced fields will disappear. In this Nernst–Planck limit there is no Kirkendall-shift (the difference of the steady state intrinsic diffusion coefficients is zero) and the intermixing is described by the $D = D_A D_B/(c_A D_A + c_B D_B)$, i.e., the slower diffusion coefficient will control the intermixing [50].

In real systems, however, more complex time evolution is expected. It can happen that the restricted efficiency of vacancy sinks leads to vacancy super saturation and porosity formation on the side of the faster component. These pores then can also sink vacancies and thus this will be a competing process with the vacancy annihilation at dislocations, i.e., with the Kirkendall-shift [51]. Furthermore, the additional diffusional stresses can enhance or suppress the porosity formation. This complex interplay of the above effects is a delicate theoretical problem and it is expected that simple analytical solutions can work only at very special simple cases even in planar geometry.

In addition, if the sample geometry is closed (cylindrical, spherical samples), since the stress-free strain fields are long-range fields, the stress development and relaxation will certainly depend on the shape and size of the sample and for example a radius dependence of the processes are also expected [50, 52, 53]. In extreme circumstances even a switching between the Darken and Nernst–Planck limits can be observed where the intermixing is controlled by the diffusion of the slower component [50, 52, 54, 55].

It was shown in [56] that if the Kirkendall-shift is negligible, a steady state Nernst–Planck regime is established with diffusion coefficient close to the slower diffusivity, independently of the type of the diffusion-induced field and also independently whether this is a single field or a combination of different fields (e.g., diffusion-induced stress field and extra chemical potential of non-equilibrium vacancies). Deviations from parabolic (Fickian) kinetics are expected only before or after this steady state stage.

It was illustrated in [57] that the setting time of the Nernst–Planck regime was very short, intermixing on the scale of few tenths of nanometer was enough to reach it.

It was also illustrated that this stage is realized even in the case of asymmetric interdiffusion, when the stress distribution has a more complex form (having a sharp peak at the interface) than in case of symmetric diffusion (see Fig. 14). Surprisingly the stress effects do not have measurable effects on the kinetic coefficient of the interface shift, i.e., the parabolic growth rate is preserved independently of the developing stress field. However, the intermixing rate decreases. The stress filed enhances the atomic flux of the slower component whereas diminishes the other. As a consequence their initial difference is equilibrated, leading to the establishment of the Nernst–Planck regime. The development of the Nernst–Planck regime is very fast, finishes before any detectable shift of the interface. This steady state stage was long enough not to reach its relaxation in the limits of the time interval investigated, although it was much longer than the stress relaxation time. This is so because the composition profile is not static but changes fast in the timescale of the stress relaxation belonging to a pure Newtonian flow and thus the stress re-develops continuously.

These are in agreement with the results in Ref. [52], where it was observed that in Al/Cu/Al and Cu/Al/Cu thin film triple layers deposited on tips of 25 nm apex radius, the growth of the reaction product was parabolic in both

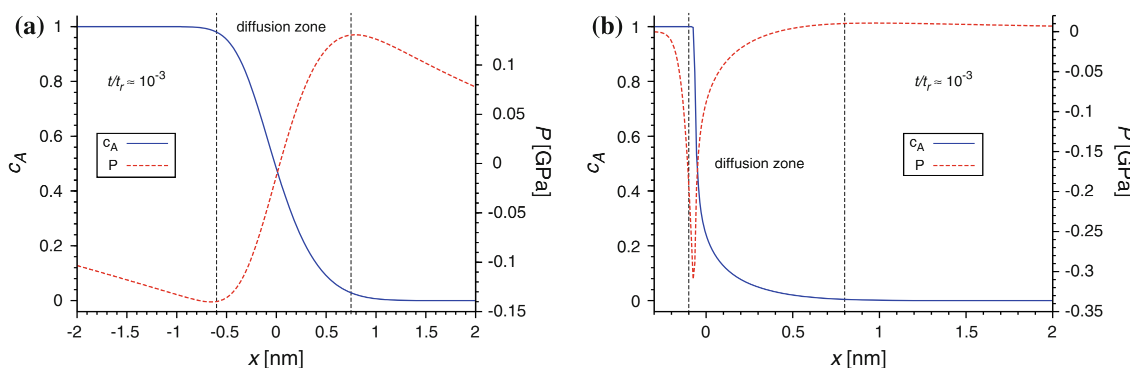

Fig. 14 Two typical, markedly different composition and pressure profiles calculated for stress-free initial conditions. **a** Composition-independent diffusion coefficients were supposed, and accordingly the profiles evolve symmetrically. **b** Strongly composition-dependent diffusion coefficients were supposed, the profiles evolves asymmetrically. If, for example, the diffusion is orders of magnitude faster in the *B* matrix than in *A*, *A* atoms can dissolve into the *B* matrix whereas *B* atoms can hardly penetrate into the *A* matrix. Consequently, a stress peak develops on the *A* side close to the interface and on the *B* side an almost homogeneous stress field (with opposite sign) appears. This sharp stress peak shifts with the moving interface (t and t_r are the time and the stress relaxation time) [57]

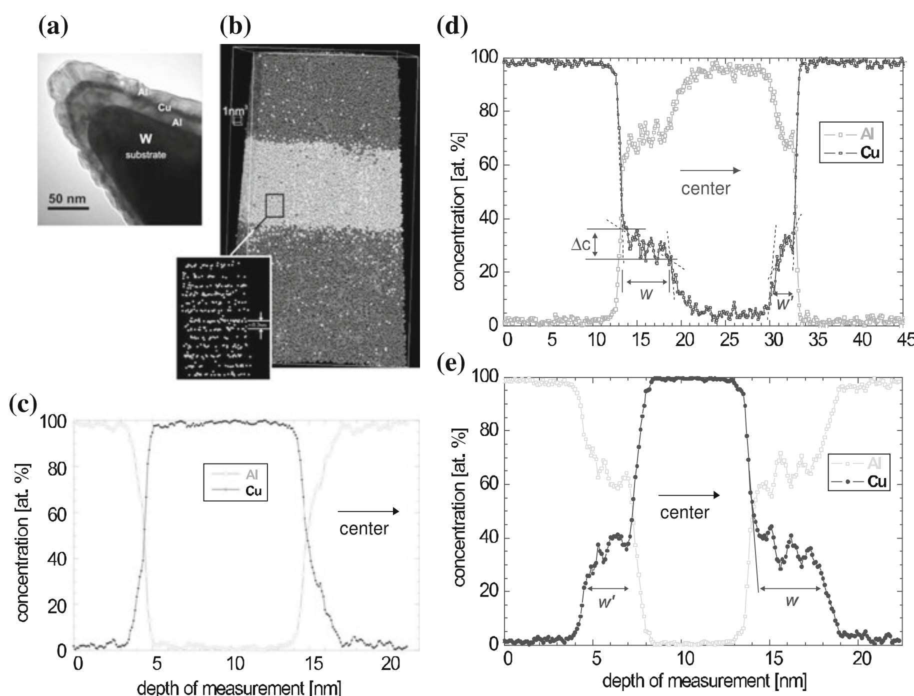

Fig. 15 Analysis of the as-prepared state of a layer sample deposited on a tungsten tip: **a** Electron micrograph. For clarity, a specimen with enlarged Al layer thickness has been chosen. **b** Tomographic reconstruction: each detected atom appears in the reconstruction as a *gray-coded dot* (*Cu* light, *Al* dark). Lattice planes are resolved inside Cu layers (*inset*). **c** Composition profile determined perpendicular to the local interfaces. Composition profiles determined perpendicular to the interfaces of **d** a Cu/Al/Cu stack and **e** of the reverse sequence Al/Cu/Al after 40 min annealing at 110 °C [52]

cases, but with remarkably different rates (see Fig. 15). This was interpreted by a switching between Darken and Nernst–Planck regimes, caused by the inhomogeneous stress inside the sample.

Furthermore, it was shown in [33], that in case of intermixing in multilayers with initially diffuse interfaces the stress effects only slowed down the interface sharpening, predicted first for stress-free case [32]. It was obtained that in the steady state regime the stress distributions were very asymmetric and a sharp stress peak developed just near the moving interface (similarly as in Fig. 14b).

Nanoscale diffusion in nanoobjects, formation of hollow nanoparticles

The precursors of hollow nanoshell formations were the experiments carried out by Aldinger [58] and by the Geguzin group [51, 59] on micrometre scale. Aldinger observed hollow shells of BeNi alloys formed from Be microparticles coated by Ni [58], while in [51, 59] hollow intermetallic wire formation in Ni coated Cd wires was described. This phenomenon was interpreted by a large change (about 8%) of the molar volume during the intermetallic phase formation in [51, 59].

While the above hollow shells or cylinders were formed in diffusion samples of micrometer dimensions, since 2004 numerous papers on hollow nanoshell formation have been published (e.g., [60–66]). Metallic spheres were reacted by oxygen and sulphur, consequently, nanoshells of oxides or sulfides were obtained (Fig. 16). In these works the formation mechanism of hollow spheres was described as an analogous phenomenon to the Kirkendall porosity formation; a nano-hole in the centre of the particles results from the generation and condensation of vacancies due to the different mobilities of ions moving in and out of the particles. It was also observed in [66] that the growth of the thickness of the oxide shell for Cu, Zn, and Al oxides had a saturation character: after an initial fast growth it reached a limiting value.

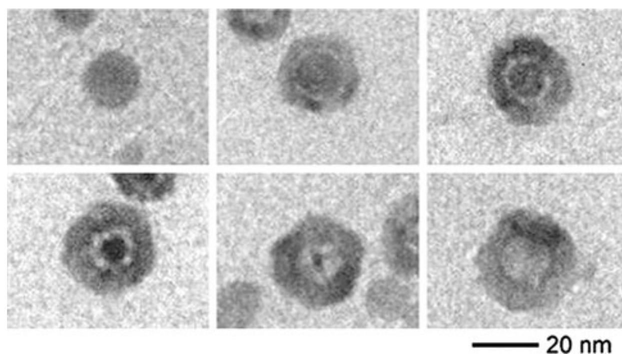

Fig. 16 Evolution of CoSe hollow nanocrystals with time by injection of a suspension of selenium in *o*-dichlorobenzene into a cobalt nanocrystal solution at 455 K, from top-*left* to bottom-*right* 0 s, 10 s, 20 s, 1 min, 2 min, and 30 min [60]

In 2005 Tu and Goesele [67] argued that such a hollow structure should be unstable due to the Gibbs–Thomson effect: the vacancy concentration on the inner boundary of the nanoshell should be higher than that on the external boundary. Thus, an outward vacancy flux is created which leads to shrinkage. In [68–70] it was argued that, contrary to the shrinking of single-component shell, shrinking of a binary compound shell should be effected by the inverse Kirkendall effect too: the outward vacancy flux leads to segregation of the faster component near the inner boundary. The corresponding concentration gradient can suppress the vacancy flux. Therefore, the shrinkage rate of the compound shell can be slowed down. The shrinkage of compound shells was experimentally verified by Nakamura et al. [71]: they observed the shrinkage of Ni and Cu oxide particles at higher temperatures than at which they where formed. In addition in [72] it was shown from model calculations that the Gibbs–Thomson effect, leading to shrinkage of ready compound shells, should be important at the formation stage as well and it may even suppress the nanoshell formation.

Up to 2010 the hollow nanoshell formation was considered—both experimentally and theoretically—only for cases when a reaction product forms the shell. Furthermore, almost exclusively only the two primary effects—vacancy flow oriented toward the centre as well as segregation—were treated. In these cases, however, the stress development caused by the abrupt change in the specific volumes during compound formation should be considerable and it was not clear what was its role in the void formation. Thus, as a first step, it was desirable to carry out experiments in which the main effect was only the oriented vacancy flow. In several theoretical papers [73–75] the problem of nanoshell formation in binary systems with complete or very wide solubility range was addressed. They have shown that first there was a relatively fast growing stage, and after a maximum in porosity, a slower shrinkage process took place.

The above theoretical predictions were experimentally verified in [76], where interdiffusion process has been studied experimentally in Ag/Au system in hemispherical geometry (Fig. 17).

Experimental techniques

As we have seen accurate knowledge of the diffusion coefficients is indispensable to understand and interpret nanoscale diffusion and reaction phenomena. Although tremendous amount of data for diffusion coefficients is available in the literature (e.g., [20, 21]), more and more

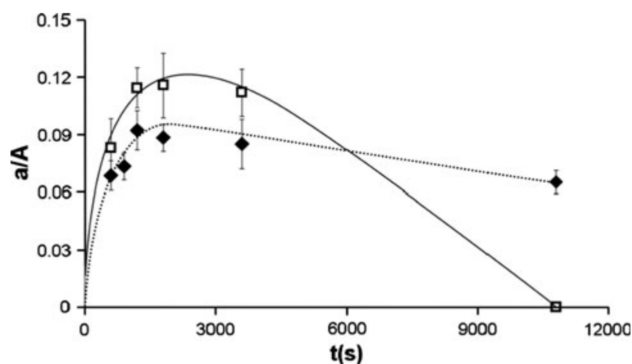

Fig. 17 Relative area of the pores as a function of the annealing time at 743 K (*open squares*) and at 723 K (*full marks*). [76]

measurements have been performed recently. Since due to the improvement of the sample preparation and measurement techniques much more accurate experiments can be performed than earlier. Atomic scale diffusion/reaction length can be detected and evaluated with great accuracy.

In this section, we will give some examples for the experimental techniques.

X-ray diffraction

X-ray diffraction (XRD) is widely used to follow phase formation in solid state reaction processes (e.g., [46, 47, 77, 78]). The main idea is that the atomic spacings are different for different materials, resulting in peaks at different angles in an XRD pattern. Accordingly, the phases grown can be identified (Fig. 18).

Moreover, the area of the peaks is proportional to the total amount of the corresponding material in the sample. Consequently, the growth of a new phase and the consumption of the parent phases can be followed if they are crystalline. In layered structures, such as multilayers, the total amount of materials is proportional to the layer thickness of the given material. This allows us to determine how the position of interfaces shifts in time (see, e.g., [47]).

From XRD patterns, composition profiles can also be reconstructed by using different models (e.g., [79, 80]). The interface sharpening mentioned in "Interface sharpening in completely miscible alloys" have been proved experimentally by analysing and reconstructing of in situ synchrotron XRD patterns [32] (Fig. 19).

X-ray and neutron reflectivity

Diffusion coefficient

One branch of the measurement aims to determine volume diffusion coefficients using multilayer samples and X-ray or neutron reflectivity technique. The basic idea dates back

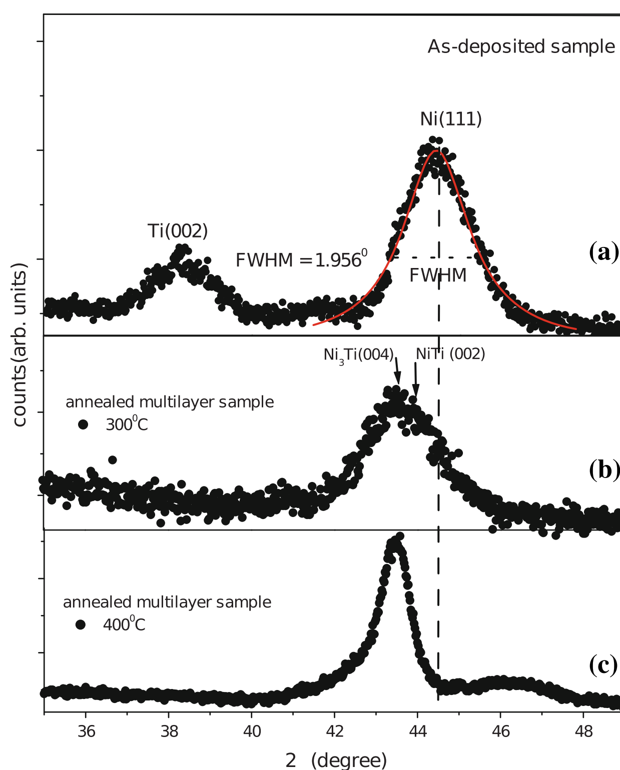

Fig. 18 **a** X-ray diffraction pattern of Ni/Ti multilayer sample from as-deposited, **b** after annealing at 300 °C, and **c** at 400 °C [77]

to 1940, when DuMond and Youtz [81] prepared their first artificial compositionally modulated material, i.e., multilayer, and observed diffusion effects in such a material. They made a thin metallic film by evaporation gold and copper on to a glass substrate by using a pendulum clock and a relay to modulate the heating current to the gold source while maintaining a constant current to the copper source. The resulting layered structure had a wavelength of about 10 nm, and they hoped that the layers would act as artificial Bragg planes for X-ray reflection. Although they found that the control of their deposition process was not adequate for this task, they did observe a Bragg reflection attributable to the composition modulation. The intensity of the reflection decreased with time, becoming about half of its initial value after 2 days at room temperature. The decay, which was due to interdiffusion in the material, was analysed by DuMond and Youtz according to the Eq. 5. They derived that for a cosinusoidal composition modulation (see Eq. 22), the intensity I of the corresponding Bragg reflection should decrease according to:

$$\frac{\mathrm{d}}{\mathrm{d}t}\left[\ln\left(\frac{I}{I_0}\right)\right] = -\frac{8\pi}{\Lambda^2}D \qquad (27)$$

which follows from Eq. 24 by multiplying it by two, and normalising by I_0, the intensity measured initially. It is seen from this equation that smaller wavelength modulations

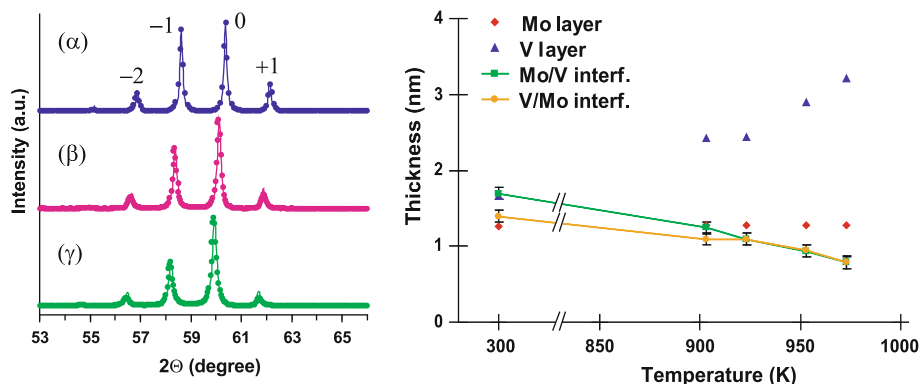

Fig. 19 *left panel* Diffraction patterns measured (*circles*) during the heat treatments and their reconstructions by the modified Stearns model (*solid line*): α room temperature, β 903 K, and γ 953 K. *a.u.* arbitrary units (*right panel*). Thickness of the interfaces as well as the pure Mo and V layers, as obtained from the fits. *Error bars* show the estimated errors of fitting. In case of the pure Mo and V layer, respectively, *error bars* are comparable to the symbol sizes. The *solid curves* are to guide the eye, *interf.* interface. [32]

will decay more rapidly. DuMond and Youtz poited out that a general periodic composition modulation can be described by a Fourier series. The higher harmonics in that series will decay rapidly, so that after some interdiffusion the fundamental will be the only significant term. That is the composition modulation will become harmonic (for instance cosinusoidal), only the first order Bragg reflection will be observed, and Eq. 27 can be used directly.

However, this is usually not true, because the composition profile do not become harmonic for example due to the composition dependence of the diffusion coefficients. It can be seen for example in Figs. 6 and 7 that the composition profiles are not cosinusoidal.

These problems, however, do not intervene using isotopically modulated multilayers, in which the chemical composition is homogeneous, only the isotope ratio of one or more constituents is modulated, e.g.,:

$$A/A^*/A/A^*/\ldots/\text{susbtrate}$$
$$A_xB_{1-x}/A^*_xB_{1-x}/A_xB_{1-x}/A^*_xB_{1-x}/\ldots/\text{susbtrate}$$
$$A_xB_{1-x}/A^*_xB^*_{1-x}/A_xB_{1-x}/A^*_xB^*_{1-x}/\ldots/\text{susbtrate}$$

where letters with and without * denote two different (usually stable) isotopes of the same element. Since in this case very high quality, stress, and (nearly) defects free samples can be grown (e.g., by molecular beam epitaxy, MBE) and as the samples are homogeneous in composition, and also remain homogeneous during the hole process, the composition dependence of the diffusivities does not play any role. Thus, for these structures the linear approximation applies, i.e., an initially square wave isotopic modulation becomes purely harmonic at the very beginning of the heat treatment and then only its amplitude decreases in time. Therefore, Eq. 24 describes its time evolution. Thus, if the time evolution of the amplitude—more exactly its square which is proportional to the intensity—can be measured isotope selectively, the diffusion coefficient can be determined by using Eq. 27.

X-ray reflectivity cannot be used to study isotopically modulated multilayers in general, as X-ray scattering cannot differentiate between two isotopes of the same element. However, isotope selectivity in X-ray scattering can be achieved in case the energy of the X-rays is tuned to the nuclear transition energy of a Mössbauer active isotope (e.g., ^{57}Fe). In such a case, total scattering amplitude from the Mössbauer isotope increases significantly due to additional contribution from nuclear resonance scattering.

The sample is, therefore, in the form of an isotopic multilayer, in which alternate layers have the same chemical compositions and differ only in the abundance of the Mössbauer isotope, e.g., ^{57}Fe. Consequently, there is no contrast between the adjacent layers as far as the X-ray scattering from the electron density in the material is concerned. However, if the energy of the incident radiation is tuned to the nuclear resonance energy of ^{57}Fe, large scattering contrast develops between layers containing natural Fe and ^{57}Fe due to strong nuclear resonance scattering from ^{57}Fe nuclei. This results in a Bragg peak in the reflectivity corresponding to the bilayer periodicity of the multilayer (see, e.g., [82]). With thermal annealing, the isotopic modulation depth of the multilayer decreases, resulting in a decrease in the intensity of the Bragg peak (see Fig. 20).

Self-diffusion coefficient of Fe in different Fe-based alloys has been determined recently using this technique with success.

Scattering of neutrons mainly takes place from nuclei, and therefore, the scattering length varies from one isotope to the other of the same element. Therefore, isotopic multilayers results in appearance of Bragg peak in neutron reflectivity. Thus, neutron reflectivity has also been used for self-diffusion measurement in isotopic multilayers

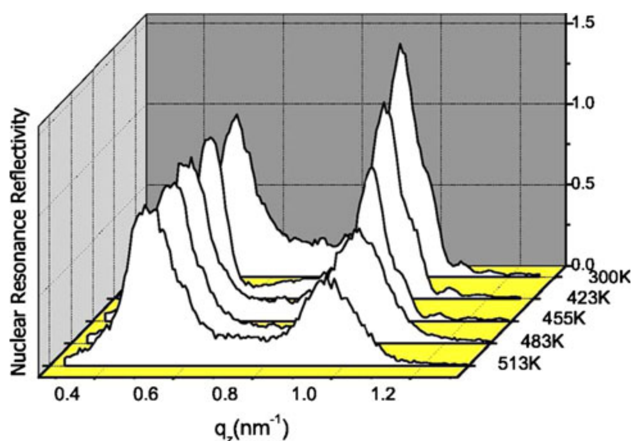

Fig. 20 Nuclear resonance reflectivity of the $^{57}Fr_{70}Zr_{30}$ /$Fe_{70}Zr_{30}$ multilayer taken at the Mössbauer resonance energy of ^{57}Fe (14.413 keV), as a function of isochronal annealing at different temperatures. The Bragg peak around $q = 0.9$ nm^{-1} corresponds to the isotopic periodicity of the multilayer [82]

(e.g., [83–86]). In contrast to the nuclear resonance reflectivity, which can be used only for Mössbauer active elements, neutron reflectivity can be used for study of self-diffusion of a larger number of elements. However, in the case of neutrons, the scattering contrast between different isotopes and hence the sensitivity, is not as high as in the case of nuclear resonance reflectivity.

Reconstruction of composition and magnetic profiles

Applying adequate algorithms (e.g., [87]), the composition profiles can also be reconstructed from reflectometry data (Fig. 21). Using polarised neutron reflectometry, magnetic profiles can also be determined (e.g., [88]).

The neutron reflectivity profile is usually fitted using a model of the depth-dependent scattering length density (SLD) profile $\rho(z)$ (where z is the film depth) with nuclear and magnetic components

$$\begin{aligned} \rho(z) &= \rho_{\text{chem}} \pm \rho_{\text{mag}}(z) \\ \rho_{\text{chem}}(z) &= \sum_i N_i(z) b_i \\ \rho_{\text{mag}}(z) &= C \sum_i N_i(z) \mu_i \end{aligned} \tag{28}$$

where the summation is over each type of atom in the system, N is the in-plane average of the number density, b is the nuclear coherent scattering length, and μ is the magnetic moment in Bohr magnetons (μ_B). The constant C is 2.69 fm/μ_B. The sign before ρ_{mag} in Eq. 28 depends on the orientation of the magnetisation relative to the neutron polarization. In the case of XRR the magnetic term is absent and the coherent scattering length b in Eq. 28 is replaced by the Thomson scattering length for X-rays, given by: $r_0(Z + f')$, where r_0 is the classical electron radius (2.8 fm), Z is the total number of electrons in the scattering atom, and f' is the dispersion term.

Depth profiling

Nowadays, with the help of modern equipments such as secondary ion mass spectrometer (SIMS), secondary neutral mass spectrometer (SNMS), or Auger electron spectroscope (AES) equipped with sputtering tools are able to reveal composition profiles with nanoscale (Fig. 7) accuracy and isotopically selectively (e.g., [22, 29, 89]). Fitting the composition profiles, diffusion coefficients can be determined (see, e.g., Fig. 22). Moreover, nanoscale shift of individual interfaces can be followed [90], from which important information concerning in diffusion or solid state processes can be obtained.

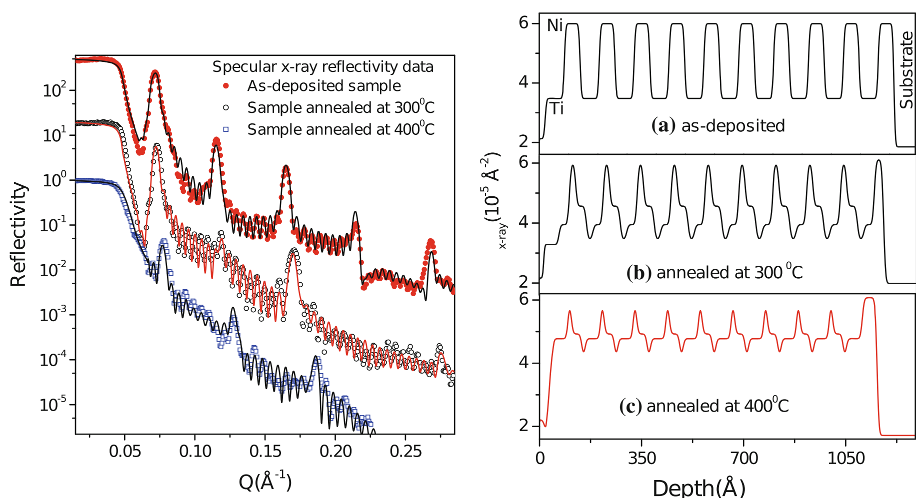

Fig. 21 *Left* X-ray reflectivity pattern for as-deposited (*closed circles*) Ni/Ti multilayer sample and sample annealed at 300 °C (*open circles*) and 400 °C (*open squares*). While *continuous lines* are fits to the corresponding measured data. *Right* The corresponding electron scattering length density depth profiles [88]

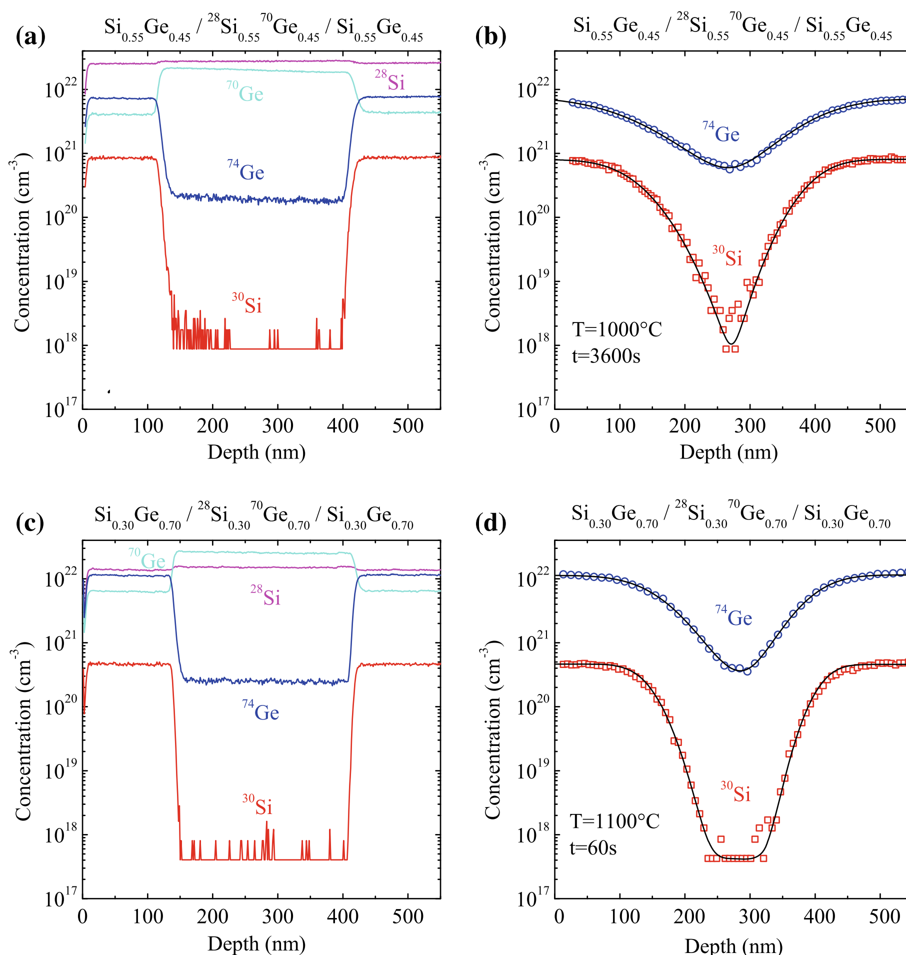

Fig. 22 SIMS concentration profiles of ^{30}Si and ^{74}Ge in the epitaxial $^{nat}Si^{nat}_{1-x}Ge_x/^{28}Si^{70}_{1-x}Ge_x/^{nat}Si^{nat}_{1-x}Ge_x$ isotope structures with $x = 0.45$ and 0.70 before (**a**, **c**) and after annealing (**b**, **d**) for temperatures and *times* indicated in the figure. The *black solid lines* are best fits based on the solution of Ficks second law of self-diffusion. For clarity only every ninth (fourth) data point are shown for Ge (Si) in (**b**, **d**) [22]

X-ray standing wave

A disadvantage of the above mentioned techniques is that they are destructive. Using, however, X-ray standing waves (XSW) depth profiles can be reconstructed from non-destructive measurements. It is a relatively new technique although the basic idea dates back to the 1970s [91–93]. Reflection on the interface between media with different refraction index is used to produce XSW. The simplest geometry requires only polished substrate and is referred as total reflection mode. In this case the incident angle is smaller than the critical angle for total external reflection, and the intensity of the reflected beam is equal to the intensity of the incoming beam. The phase difference between incoming and reflected beam depends only on the distance from the sample surface. Figure 23 shows the interference patterns above the total reflecting sample.

As considerable interaction between the beam and the matter (i.e., the sample to be measured) on the substrate can take place only in the region of high electric field power, it can be used to gain depth selective information form the sample. The reflectivity at higher angles can be improved by using the reflection on multilayer instead of total external reflection [95–97]. Using this geometry, e.g., asymmetric diffusion at the interfaces in Fe/Si multilayers was shown [98]. The asymmetry was explained by peculiarities during Si/Fe/Si layer formation by sputter deposition, in particular due to the difference between the surface free energies of Fe and Si. Further amplification of the

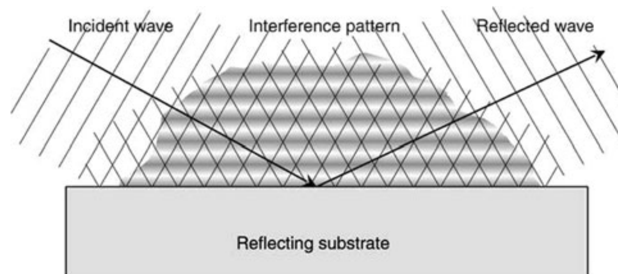

Fig. 23 Formation of the interference (XSW) pattern above the reflecting surface. An incoming and reflected wave are represented using *lines* of constant phase, i.e., wave fronts. Since both waves are in phase, the path difference and the phase shift depend on the height above surface. The resulting electric field above the surface is the sum of the electric fields of both beams, resulting in the higher power density in regions where the two beams are in phase. *Gray* scale pattern in the background describes the electric field power (*higher values are dark*) [94]

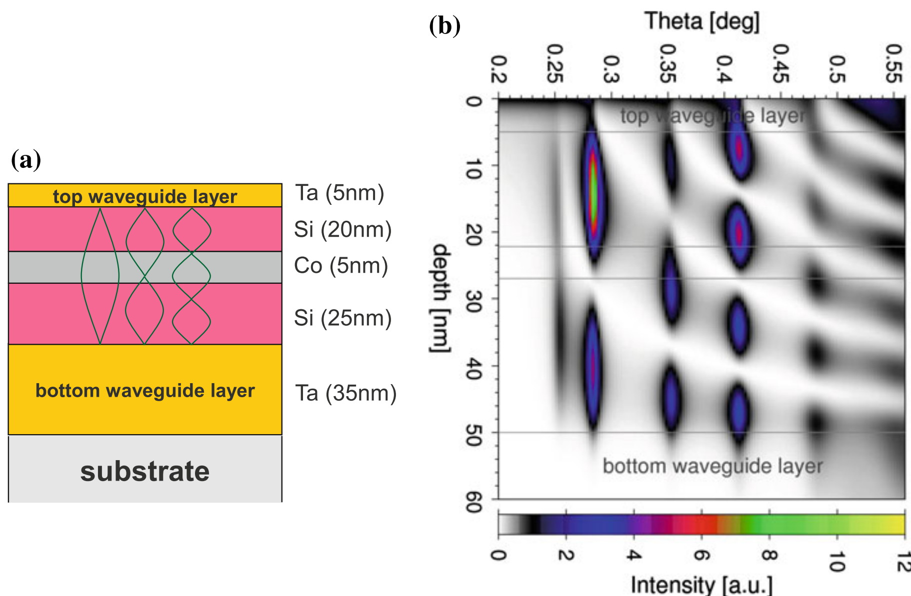

Fig. 24 **a** Waveguide sample structure developed to study the early stage of solid state reaction in Co–Si system. The *Ta* layers are the reflectors, *Si* is the spacer; the Si/Co/Si trilayer is the sample to be investigated. The schemes of the first three transverse electric mode (TE) are also illustrated. **b** Intensity plot of the calculated electric field. The different TE as a function of the incident angle is displayed [99]

intensity pattern can be achieved putting the sample in the space between two reflecting layers. If the refraction index of the reflector material is significantly larger than that of the spacer material, the beam is going to be bounced from the walls several times before being absorbed. The multiply reflected beam is going to interfere with itself, and at certain incident beam angles the electric field may form standing wave-like patterns (Fig. 24).

To determine the element distribution through the layer, the incident angle is scanned by constant energy and fluorescence of different elements is measured. The result is fitted to fluorescence calculated by a model assuming an element distribution [99]. Figure 25 shows the reconstructed distribution of Co at the as-deposited sample and after 3 h annealing at 500 K.

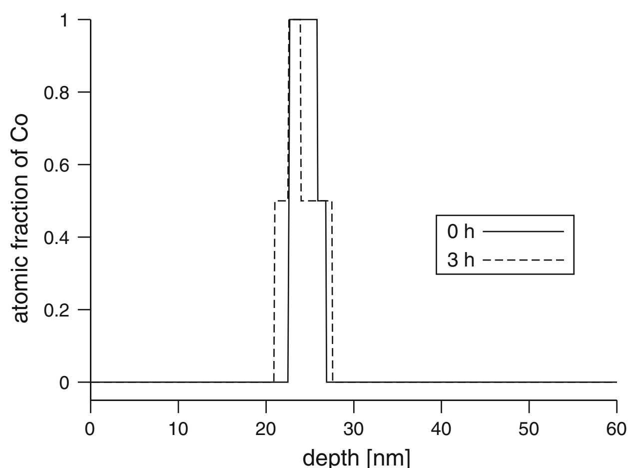

Fig. 25 The *plateaus* in the distribution indicate CoSi phase. At the beginning, the interfaces of the Co layer are very sharp, except for a very thin layer containing 50 at.% Co at the lower interface. After annealing the layers containing 50 at.% Co are present on both interfaces, and are much thicker than at the beginning [99]

To collect more information on the inter-metallic phase the EXAFS (extended X-ray absorption fine structure) measurement can also be performed in this geometry. It allows to determine the average distance between Si–Co nearest neighbours an the average number of Si neighbors of a Co atom. On the basis of these data, one can decide if the plateaus in the element distribution corresponds to real CoSi ordered phase or a mixture of Co and Si atoms [99]. Fe and W marker layers in Si were investigated in a very similar way [100]. This method is referred in the literature as GIXRF (grazing incidence X-ray fluorescence analysis) analysis and EXAFS spectroscopy in fluorescence detection with X-ray standing waves (XSW) technique.

Atom probe tomography

Atom probe tomography enables the quantitative chemical analysis of nanostructured materials on a nearly atomic scale (see Fig. 15). By carefully controlled field evaporation, individual atoms are removed from a tip-shaped sample and their time of flight and impact positions are determined. Using these data the atoms are identified by mass spectroscopy and also their geometric origin within the specimen is reconstructed. Offering the possibility of mapping the three-dimensional (3D) arrangement of individual atoms, the method can be used to investigate phenomena on the smallest length scales important in material science. In atom probe tomography, individual atoms or molecules are removed from the surface by applying high electric fields of several volts per nanometer. The required field strength can be achieved with reasonable voltage, if

needle-shaped specimens with a tip radius below 100 nm are used. In laser-assisted atom probe technique (see, e.g., [101]), the HV pulse is replaced by a short laser pulse, which offers the ability to expand the range of analysed materials to poorly conducting or insulating materials such as oxides, glasses, ceramics, and polymeric materials. Since atom probe tomography technique allows one to reconstruct the position of individual atoms, it is an important tool in diffusion research on the nanoscale (see, e.g., [52, 102–104]).

Acknowledgements This study was supported by the OTKA Board of Hungary (Nos K67969, CK80126) and by TAMOP 4.2.1./B-09/1/KONV-2010-0007 project (implemented through the New Hungary Development Plan co-financed by the European Social Fund, and the European Regional Development Fund). One of the authors (Z. Erdélyi) of this article is a grantee of the 'Bolyai János' scholarship.

References

1. Fick AE (1855) Ann Phys Chem 94:59
2. Fick AE (1855) Phil Mag 10:30
3. Crank J (1975) In: The mathmatics of diffusion. Oxford Univerity Press, Oxford
4. Philibert J (1991) In: Atom movements: diffusion and mass transport in solids. Les Editions de Physique, Les Ulis
5. Mehrer H (2007) In: Diffusion in solids. Springer-Verlag, Berlin
6. Martin G (1990) Phys Rev B 41:2279
7. Yip S (eds) (2005) In: Handbook of materials modeling. Springer, Dordrecht
8. Stephenson G (1988) Acta Metall 36(10):2663
9. Stephenson G (1993) Def Diff Forum 95(98):507
10. Manning JR (1968) In: Diffusion kinetics for atoms in crystals D. Van Norstrand Company Inc., Princton
11. Ghez R (2001) In: Diffusion phenomena. Kulwer Academic/Plenum Publishers, New York
12. Erdélyi Z, Beke DL (2004) Phys Rev B 70:245428
13. Cook H, de Fontaine D, Hilliard J (1969) Acta Metall 17:165
14. Cahn J (1972) Acta Metall 9:795
15. Yamautchi H, Hilliard J (1972) Scr Metall 6:909
16. Tsakalakos T (1981) Thin Solid Films 86:79
17. Tsakalakos T (1986) Scr Metall 20:471
18. Memon E, de Fontaine D (1992) Scr Metall 27:395
19. Erdélyi Z, Beke D, Nemes P, Langer G (1999) Phil Mag A 79:1757
20. Mehrer, H (eds) (1990) In: Diffusion in solid metals and alloys, Landolt-Börnstein, New Series, vol III/26. Springer-Verlag, Berlin
21. Beke, D (eds) (1999) In: Diffusion in semiconductors and nonmetallic solids, Landolt-Börnstein, New Series, vol III/33. Springer-Verlag, Berlin
22. Kube R, Bracht H, Hansen JL, Larsen AN, Haller E, Paul S, Lerch W (2010) J Appl Phys 10:073520
23. Bracht H (2006) Physica B 367(377):11
24. Bracht H, Haller E, Clarck-Phelps R (1998) Phys Rev Lett 81:393
25. Silvestri HH, Bracht H, Hansen JL, Larsen AN, Haller EE (2006) Semicond Sci Technol 21:172103
26. Hüger E, Tietze U, Lott D, Bracht H, Bougeard D, Haller EE, Schmidt H (2008) Appl Phys Lett 93:162104
27. Erdélyi Z, Balogh Z, Beke D (2010) Acta Mater 58:5639
28. Beke DL, Cserháti C, Erdélyi Z, Szabó IA (2003) In: Nanoclusters and nanocrystals. American Scientific Publ., Califronia
29. Csik A, Langer G, Beke D, Erdélyi Z, Menyhard M, Sulyok A (2001) J Appl Phys 89:804
30. Tripathi S, Sharma A, Shripathi T (2009) Appl Surf Sci 256:489
31. Erdélyi Z, Szabó IA, Beke DL (2002) Phys Rev Lett 89:165901
32. Erdélyi Z, Sladecek M, Stadler LM, Zizak I, Langer G, Kis-Varga M, Beke D, Sepiol B (2004) Science 306:1913
33. Erdélyi Z, Beke DL (2003) Phys Rev B 68:092102
34. Roussel JM, Bellon P (2006) Phys Rev B 73:085403
35. Klafter J, Sokolov I (2005) Phys World 18:29
36. Philibert J (2009) Int J Mater Res 100:744
37. Sokolov I, Klafter J, Blumen A (2002) Phys Today 55:48
38. Erdélyi Z, Katona GL, Beke DL (2004) Phys Rev B 69:113407
39. Beke DL, Erdélyi Z (2006) Phys Rev B (Condens Matter Mater Phys) 73:035426
40. Katona GL, Erdélyi Z, Beke DL, Dietrich C, Weigl F, Boyen HG, Koslowski B, Ziemann P (2005) Phys Rev B 71:115432
41. Erdélyi Z, Girardeaux C, Tőkei Z, Beke D, Cserháti C, Rolland A (2002) Surf Sci 496:129
42. Balogh Z, Erdélyi Z, Beke D, Wiedwald U, Pfeiffer H, Tschetschetkin A, Ziemann P (2011) Thin Solid Film (in press)
43. Balogh Z, Erdélyi Z, Beke D, Langer G, Csik A, Boyen HG, Wiedwald U, Ziemann P, Portavoce A, Girardeaux C (2008) Appl Phys Lett 92:143104
44. d'Heurle F, Gas P (1986) J Mater Res 1:205
45. Gas P, d'Heurle F (1988) In: Landolt-Börnstein new series, vol III 33A. Springer, Beriln
46. Nemouchi F, Mangelinck D, Berman C, Gas P (2005) Appl Phys Lett 86:041903
47. Cserháti C, Balogh Z, Csik A, Langer G, Erdélyi Z, Glodán G, Katona G, Beke D, Zizak I, Darowski N, Dudzik E, Feyerherm R (2008) J Appl Phys 104:024311
48. Portavoce A, Tréglia G (2010) Phys Rev B 82:205431
49. Erdélyi Z, Beke DL, Taranovskyy A (2008) Appl Phys Lett 92:133110
50. Beke D, Szabo I, Erdélyi Z, Opposits G (2004) Mater Sci Eng A 387(389):4
51. Geguzin Y (1979) In: Diffusion zone. Nauka, Moscow
52. Schmitz G, Ene C, Nowak C (2009) Acta Mater 57:2673
53. Beke D, Kozéky L, Gödény I, Kedves F (1989) Def Diff Forum 66(69):1357
54. Bokstein B, Bokstein S, Zsukhovicki A (1974) Metallurgica 66(69):169
55. Nazarov AV, Gurov KP (1974) Fiz Metall Metalloved 37:496
56. Beke DL, Erdélyi Z, Parditka B (2011) Def Diff Forum 309 (310):113
57. Erdélyi Z, Parditka B, Beke D (2011) Scr Mater 64:938
58. Aldinger A (1974) Acta Metall 22:923
59. Geguzin Y, Klinchuk Y, Yu I, Paritskaya L (1977) Fiz Met Metalloved 43:602
60. Yin Y, Rioux RM, Erdonmez CK, Hughes S, Somorjai GA, Alivisatos AP (2004) Science 304:711
61. Yin Y, Erdonmez CK, Cabot A, Hughes S, Alivisatos AP (2006) Adv Func Matt 16:1389
62. Wang CM, Baer D, Thomas L, Amonette J, Antony J, Qiang Y, Duscher G (2005) J Appl Phys 98:09430
63. Nakamura R, Lee JG, Tokozakura D, Mori H, Nakajima H (2007) Matter Lett 61:1060
64. Nakamura R, Tokozakura D, Nakajima H, Lee JG, Mori H (2007) J Apll Phys 101:074303
65. Nakamura R, Lee JG, Mori H, Nakajima H (2008) Phil Mag 88:257
66. Nakajima H, Nakamura R (2009) J Nano Res 7:1
67. Tu KN, Gosele U (2005) Appl Phys Lett 86:093111

68. Gusak AM, Zaporozhets T, Tu K, Gosele U (2005) Phil Mag 85:4445
69. Belova I, Murch G (2005) J Phase Equil Diff 26:430
70. Evteev A, Levchenko E, Belova I, Murch G (2007) Phil Mag 87:3787
71. Tokozakura RND, Lee J, Mori H, Nakajima H (2008) Acta Mater 56:5276
72. Gusak AM, Tu K (2008) Acta Mater 57:3367
73. Evteev A, Levchenko E, Belova I, Murch G (2009) J Nano Res 7:11
74. Evteev A, Levchenko E, Belova I, Murch G (2008) Phil Mag 88:1524
75. Gusak AM, Zaporozhets TV (2009) Condens Matter 21:415303
76. Glodan G, Cserhati C, Beszeda I, Beke DL (2010) Appl Phys Lett 97:113109
77. Singh A, Basu A, Bhatt P, Poswal A (2009) Phys Rev B 79:195435
78. Knaepen W, Demeulemeester J, Deduytsche D, Jordan-Sweet J, Vantomme A, Meirhaeghe RV, Detavernier C, Lavoie C (2010) Microelect Eng 87:258
79. Sterns MB (1988) Phys Rev B 38:8109
80. Fullerton EE, Schuller IK, Vanderstraeten H, Bruynseraede Y (1992) Phys Rev B 45:9292
81. DuMond J, Youtz J (1940) J Appl Phys 11:357
82. Gupta A, Gupta M, Chakravarty S, Ruffer R, Wille HC, Leupold O (2005) Phys Rev B 72:014207
83. Gupta A, Gupta M, Pietsch U, Ayachit S, Rajagopalanl S, Balamurgan A, Tyagi A (204) J Non-Cryst Solids 343:39
84. Speakman J, Rose P, Hunt J, Cowlam N, Somekh R, Greer A (1996) J Magn Magn Mater 156:411
85. Schmidt H, Gupta M, Bruns M (2006) Phys Rev Lett 96:055901
86. Gupta M, Gupta A, Stahn J, Horisberger M, Gutberlet T, Allenspach P (2004) Phys Rev B 70:184206
87. Parratt LG (1954) Phys Rev 95:359
88. Singh S, Basu S, Gupta M, Majkrzak CF, Kienzle PA (2010) Phys Rev B 81:235413
89. Cekada M, Panjan M, Cimpric D, Kovac J, Panjan P, Dolinsek J, Zalar A (2010) Vacuum 84:147
90. Lakatos A, Langer GA, Csik A, Cserháti C, Kis-Varga M, Daróczi L, Katona GL, Erdélyi Z, Erdélyi G, Vad K, Beke DL (2010) Appl Phys Lett 97(23):233103
91. Batterman B (1969) Phys Rev Lett 22:703
92. Anderson S, Golovchenko J, Mair G (1976) Phys Rev Lett 37:1141
93. Cowan P, Golovchenko J, Robbins M (1980) Phys Rev Lett 44:1680
94. Erko A, Zizak I (2009) Spectrochim Acta Part B Atom Spectrosc 64:833
95. Erko A, Veldkamp M, Gudat W, Abrosimov N, Rossolenko S, Shekhtman V, Khasanov S, Alex V, Groth S, Schröder W, Vidal B, Yakshin A (1998) J Synchrotron Radiat 5:239
96. Ghose S, Dev B, Gupta A (2001) Phys Rev B 64:233
97. Ghose S, Dev B (2001) Phys Rev B 63:245409
98. Gupta A, Kumar D, Phatak V (2010) Phys Rev B 81:155402
99. Erdélyi Z, Cserháti C, Csik A, Daróczi L, Langer G, Balogh Z, Varga M, Beke D, Zizak I, Erko A (2009) X-ray Spectrom 38:338
100. Gupta A, Rajput P, Saraiya A, Reddy VR, Gupta M, Bernstorff S, Amenitsch H (2005) Phys Rev B 72:075436
101. Schlesiger R, Oberdorfer C, Wurz R, Greiwe G, Stender P, Artmeier M, Pelka P, Spaleck F, Schmitz G (2010) Rev Sci Instrum 81:043703
102. Stender P, Balogh Z, Schmitz G (2011) Phys Rev B 83:121407
103. Cojocaru-Mirédin O, Cadel E, Blavette D, Mangelinck D, Hoummada K, Genevois C, Deconihout B (2009) Ultramicroscopy 109:797
104. Adusumilli P, Lauhon LJ, Seidman DN, Murray CE, Avayu O, Rosenwaks Y (2009) Appl Phys Lett 94:113103